Acta Astronautica 226 (2025) 71–86

Contents lists available at ScienceDirect

Acta Astronautica

journal homepage: www.elsevier.com/locate/actaastro

Research paper

In-orbit system identification of a flexible satellite with variable mass using dual Unscented Kalman filters

Alex J. Elliott [a,*], Aydin Nakhaeezadeh Gutierrez [a,b], Leonard Felicetti [a], Luca Zanotti Fragonara [a]

[a] School of Aerospace, Transport and Manufacturing, Cranfield University, Cranfield, UK
[b] Department of Computer Science, Electrical and Space Engineering, Lulea University of Technology, Kiruna, Sweden

ARTICLE INFO

Keywords:
Satellite dynamics
In-orbit system identification
Flexible satellite
Dual Unscented Kalman filter

ABSTRACT

Modern space mission concepts are increasingly dependent on the robust and reliable deployment of spacecraft with large appendages, such as antennas, booms or solar panels. Such deployment requires the ability to properly capture and control the coupled system dynamics, which requires accurate in-orbit system identification of the mass and structural properties. This paper utilises dual Unscented Kalman filters (DUKF) to develop an online system identification strategy that captures both the structural and mass properties, and the attitude and orbit dynamics. The dynamics of the flexible multibody problem are derived from the Lagrangian equations, with the flexible body characteristics modelled with finite element software. A genetic algorithm is used to optimise the accelerometer placement, and hence improve the DUKF performance. We demonstrate that this approach can accurately capture the coupled attitude, orbit, and structural dynamics, as well as being able to provide in-orbit updates for mass properties such as the moment of inertia. The methodology is explored for two illustrative cases: one in which the initial moment of inertia is incorrectly characterised, one in which the moment of inertia changes with time. In both cases, the DUKF approach captures both the system dynamics and the mass properties, which are captured with an error of less than 1%.

1. Introduction

Identifying and modelling the mass and structural properties of spacecraft represents a key challenge for the design of accurate and reliable attitude and orbit control systems (AOCS) [1,2]. In some cases, the true values of these properties can differ from those obtained from finite element (FE) software due to material imperfections or floating components that are not easily predicted with mathematical models. Similarly, structural parameters determined via on-ground experiments can have high degrees of uncertainty as a result of external factors such as gravity and air friction [3].

This challenge of developing accurate AOCS is increased when the mass and structural spacecraft change during the mission lifetime, for example, as a result of propellant consumption during orbital manoeuvre [4]. Furthermore, modern spacecraft configurations often include deployable elements, moving masses, and flexible appendages, all of which could induce changes in the mass and inertia configuration of the spacecraft during the mission [5]. Recent telecommunication mission concepts, including Vasant [6] and INMARSAT-4 [7], utilise large, lightweight telecommunication antennas and solar arrays to improve the capacity and resilience of their satellites. The additional benefit of these appendages is dependent on the ability of the AOCS design to accurately capture and control the higher level of deformation observed in such large structures [8]. Spacecraft of an even greater scale have been considered for space-based solar power applications [9,10], with typical designs including high-aspect ratio appendages at the kilometre length scale. When designs are this slender, lightweight, and flexible, it is likely that the vibrations can no longer be accurately captured with linear models, with the vibrations instead being in the nonlinear region [11]. Although this paper considers only linear vibrations, this trend towards increasingly large structures and flexible appendages highlights the importance of AOCS that are capable of accurately capturing the structural dynamics and integrating them into the control strategy.

High fidelity models and control systems for the dynamics of a satellite with flexible appendages have long been sought within the field of structural dynamics [2,12,13]. Typically, multibody formulations are found using one of three approaches, namely the Newton–Euler [14], Euler–Lagrange [15] and Kane [16] methods. In the Newton–Euler method, the dynamic equations for each particle are defined separately and then coupled via links for which the dynamic behaviour is defined. Instead, the Euler–Lagrange method derives the equations of motion of the full system based on its contained energy, which does not require

* Corresponding author.
E-mail address: Alex.J.Elliott@cranfield.ac.uk (A.J. Elliott).

https://doi.org/10.1016/j.actaastro.2024.11.014
Received 24 April 2024; Received in revised form 27 September 2024; Accepted 5 November 2024
Available online 16 November 2024
0094-5765/Crown Copyright © 2024 Published by Elsevier Ltd on behalf of IAA. This is an open access article under the CC BY license (http://creativecommons.org/licenses/by/4.0/).

the inclusion of constraint equations. Finally, Kane's method introduces a Jacobian matrix to relate the Lagrangian velocity variables to Newtonian ones, allowing the minimum number of ordinary differential equations capable of fully describing the multibody dynamics to be found without the need to consider forces between interconnected bodies. These strategies have an established track record for developing models for flexible satellites [1,17–20] and this continues to be an active research area. Flexible solar panels are modelled as Euler–Bernoulli beams in [21] and are controlled using a single-point control force. A similar modelling approach has also been used to investigate active vibration suppression [22], disturbance-observer-based control [23], and a nonlinear reduced-attitude control law [24]. Across these examples, the exclusion of torsional modes prevents their immediate application in real-world applications.

While these works simplify the flexible appendage model by assuming the deformations are in-plane, other studies have explored more realistic three-dimensional models. The authors of [25,26] explore the impact of uncertainties for AOCS through the application of a nonlinear attitude controller, which was shown to be effective in controlling the attitude, though not for the vibrations of the flexible appendages. In [27,28], inverse simulation is instead used to control the structure, showing strong abilities in controlling the attitude dynamics and advising on feasible manoeuvres, though still underperforming in quaternion tracking and pointing error reduction. The authors of [29] applied an estimation-based strategy with fast fixed-time observer for reconstructing the uncertain dynamics and robust fixed-time controller, through which they were able to achieve fixed-time system state convergence despite actuator uncertainty. Model predictive control has also been successfully applied to spacecraft with flexible rotation in [30,31], with the former utilising a genetic algorithm to optimise controller performance.

A key aim of the present study is to design an in-orbit system identification strategy that is capable of accurately capturing the inertia properties of an in-orbit satellite. As discussed above, modern spacecraft configurations include flexible appendages, adaptive elements, and fuel expenditure during manoeuvres, all of which can impact the ability to accurately capture the inertia. Previous research in this area initially focused on inertia property identification for spacecraft with robotic arms [32,33]. In recent years, a greater emphasis has been placed on the inertia of small satellites, including through the use of instrumental variable approaches [34], deep neural networks [35], and least squares methods [36]. However, across these recent investigations, it is implicitly assumed that the impact of flexible appendages is negligible. The methodologies also aim to identify a fixed moment of inertia matrix, which is not guaranteed if the system uses thruster to perform attitude manoeuvres [4].

The application of sequential filtering techniques has largely revolved around the use of Kalman filters [37], including derivatives such as the Extended Kalman filter (EKF) [38] and Unscented Kalman filter (UKF) [39]. The application of Kalman filters to estimate the attitude and modal dynamics of satellites is more established than for subspace identification methods, with [40] achieving accurate predictions for the attitude and structural dynamics of a satellite model with single-degree-of-freedom flexible appendage. EKF-based methods have been used for attitude identification of CubeSats [41] and rigid body satellites more generally [42], with [43] offering adaptations to the strategy that resulted in improved robustness. A robust EKF strategy was also developed in [44] through the application of multiple scale factors, and the strategy was also demonstrated to be beneficial in the development of a robust UKF strategy. The authors of [45] also focused on improving robustness, this time utilising robust cubature to increase accuracy and stability.

Kalman filters have also been used in the identification of flexible structures, including the use of both EKF and UKF to estimate the attitude and deformation dynamics [46], and an observer/Kalman filter identification algorithm to identify microvibrations [47]. This concept has also been expanded, in [48], to provide attitude control of combined spacecraft, though flexible appendages are not included here. Finally, [49] utilises a vanilla Kalman filter-based approach to identify the inertial properties of a large-scale flexible spacecraft; the paper achieved errors below 10% in the considered cases.

Table 1
System parameters for the flexible satellite model.

Parameter	Magnitude	Parameter	Magnitude
Rigid body:			
Dimensions	0.5 × 0.5 × 0.5 m	Mass	500 kg
CoM	(0, 0, 0) m	I_{xx}	20.83 kg m^2
I_{yy}	20.83 kg m^2	I_{zz}	20.83 kg m^2
Solar panels:			
Dimensions	1.5 × 0.5 × 0.0062 m	Mass	12.65 kg
I_{xx}	0.84 kg m^2	I_{yy}	14.44 kg m^2
I_{zz}	13.86 kg m^2	I_{xy}	0 kg m^2
I_{xz}	299 kg m^2	I_{yz}	0 kg m^2

The application of dual Unscented Kalman filters (DUKF) for attitude state and parameter estimation was pioneered in [50]. This approach allows for the system state and model parameters to be updated in parallel, enabling a more complete system identification. A similar approach was presented in [51] to better facilitate low-precision sensors through the addition of a second gain matrix that accounts for the measurement residuals of the previous time step. Note that the two gain matrices used in [51] are both applied for state estimation, whereas [50] estimates both the state and parameter estimation. The notion of applying two UKFs has also been developed through the two-stage UKF (TUKF), pioneered in [52]. The TUKF estimates not only the system state, but also the value of an unknown random bias. The method has been applied for estimating faults in the actuator and sensors for a spacecraft attitude control system [53], as well as for estimating battery charge [54].A similar two-stage method, which utilises a cubature KF, rather than UKF, was developed in [55], and subsequently applied as a target tracking algorithm [56].

The work presented in this paper builds upon the DUKF approach in [50], but with the additional challenge of identifying both the displacement state of flexible appendages, and the mass and inertia dynamics of the satellite. While TUKF utilises an additional bias term to correct for systematic errors in the state model, the DUKF approach outlined here allows for the value of specific structural parameters (i.e., the inertia) to be directly estimated. This is an important skill for spacecraft that cannot be fully characterised prior to launch.

This paper is organised as follows. Section 2 reviews the dynamic model for the coupled system, including validation. Section 3 outlines the measurement system used for the satellite and presents a novel structural health monitoring-inspired approach for accelerometer placement. In Section 4, the DUKF identification system for a flexible satellite, and Section 5 assesses this approach through the application of two case studies: one in which the initial moment of inertia matrix is inaccurate, the other in which the true inertial values decay, mimicking the expenditure of fuel in operation. Conclusions are drawn and future extensions of this work are presented in Section 6.

2. Flexible satellite model

The flexible satellite considered in this study is presented in Fig. 1, along with the reference coordinate frames used in the modelling process. It consists of a rigid, cubic body with two flexible solar panels rigidly attached at the base on opposite sides. The system parameters are defined in Table 1.

The model of the flexible satellite considered in this paper uses a mixed set of equations of motion, derived from the Lagrangian of the

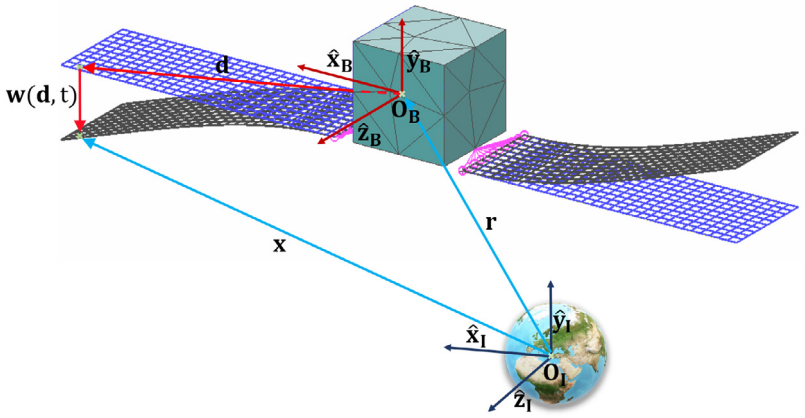

Fig. 1. Flexible body state representation.

system.[1] This approach allows the structural models of the components of the satellite developed using FE software tools to be easily integrated, as will be outlined in Section 2.3.

In the following subsections, a brief overview of the equations that define both the kinematics and dynamics of the flexible satellite is presented. These sections will define the reference frames, terminology, and assumptions made to develop both the simulation tools and estimation algorithms that form the novelty of this research.

2.1. Kinematics

Fig. 1 illustrates the flexible satellite in orbit, and defines the reference frames that will be adopted within the subsequent theoretical development and simulations. The satellite is composed of a central mass, which is considered as a rigid body, and two flexible solar panels.

The surface of the flexible appendages is spanned by the vector $\mathbf{d}$, which is defined in terms of the undeformed configuration of the satellite in the Body Reference Frame (BRF). The time-dependent deflection of the panels is denoted $\mathbf{w}(\mathbf{d}, t)$ and decomposed using a Galerkin decomposition in terms of the mass-normalised mode shapes[2] of the structure (in m), $\phi_k(\mathbf{d})$, and time-varying, dimensionless scale factors, $A_k(t)$, that quantify the "contribution" of each mode shape to the overall displacement. Now, the deformed position of points along the satellite are given in the Earth Centerd Inertial (ECI) reference frame as [8]:

$$\mathbf{x} = \mathbf{x}_0 + \mathbf{T}\left(\mathbf{d} + \sum_{k=1}^{N_n} A_k(t)\phi_k(\mathbf{d})\right), \tag{1}$$

where $\mathbf{x}_0$ denoted the position of the origin, and $\mathbf{T}$ is used to rotate the coordinates of both $\mathbf{d}$ and $\mathbf{w}(\mathbf{d}, t)$ from the BRF to the ECI reference frame.

The full system dynamics are then defined by the generalised Lagrangian coordinate vector, $\psi = [\mathbf{x}_0 \;\; \theta \;\; \mathbf{A}]^{\mathrm{T}}$, which comprises the orbit position of the full-satellite centre of mass ($\mathbf{x}_0$), the body attitude, defined in terms of the Euler angles (θ), and the modal coordinates of the flexible appendages ($\mathbf{A}$).

[1] A full derivation of these equations is omitted for the sake of brevity, but is readily available in, for example, [8].

[2] The first six mode shapes are presented in Appendix A.

2.2. Dynamics

The dynamic model for the flexible satellite system is derived from the Lagrangian of the system, defined by

$$\mathcal{L} = \mathcal{T} - \mathcal{V}, \tag{2}$$

where $\mathcal{T}$ and $\mathcal{V}$ denote the kinetic and potential energy of the system, respectively.

The kinetic energy is given in terms of the kinematics of the rigid body ($_b$) and flexible appendage ($_f$):

$$\mathcal{T} = \frac{1}{2}\int_{m_b} \dot{\mathbf{x}}_b^{\mathrm{T}}\dot{\mathbf{x}}_b \rho_b dV_b + \frac{1}{2}\int_{m_f} \dot{\mathbf{x}}_f^{\mathrm{T}}\dot{\mathbf{x}}_f d\rho_f V_f, \tag{3}$$

where both integrals are defined over the volume, V, of the respective component.

The potential energy is defined as the sum of the elastic and gravitational potentials:

$$\begin{aligned}\mathcal{V} &= \frac{1}{2}M\sum_{k=1}^{N_n} A_k(t)^2\omega_k^2 - \mu\int_V \frac{\rho}{|\mathbf{x}|}dV \\ &= \frac{1}{2}M\sum_{k=1}^{N_n} A_k(t)^2\omega_k^2 - \frac{\mu}{|\mathbf{x}_0|}\left[m - \frac{\tilde{\mathbf{p}}\hat{\boldsymbol{k}}}{|\mathbf{x}_0|} + \frac{1}{|\mathbf{x}_0|^2}\left[\mathrm{tr}(\mathbf{I}) - \mathbf{I} - 3\left(\hat{\boldsymbol{k}}^{\mathrm{T}}\tilde{\mathbf{I}}\hat{\boldsymbol{k}}\right)\right]\right],\end{aligned} \tag{4}$$

where M, V, ρ are the body mass, volume, and density, respectively. ω_k denotes the k^{th} natural frequency of the structure.

The expression defined in Eq. (2) can be directly applied in the Lagrangian equations, the i^{th} of which is defined by

$$\frac{d}{dt}\frac{\partial\mathcal{L}}{\partial\dot{\psi}_i} - \frac{\partial\mathcal{L}}{\partial\psi_i} = Q_i. \tag{5}$$

Applying the energy definitions given in Eqs. (3) and (4) in Eq. (5) leads to the following governing equations for the flexible satellite:

$$\begin{aligned} M\ddot{\mathbf{x}}_0 &= \boldsymbol{\mathcal{F}}_G \\ \tilde{\mathbf{I}}\dot{\boldsymbol{\omega}} + \sum_{m=1}^{N_m}\left[\bar{\mathbf{I}}_1{}^m\boldsymbol{\omega}\dot{A}_m + \bar{\boldsymbol{\Gamma}}_m\ddot{A}_m\right] + \boldsymbol{\omega}\times\left[\tilde{\mathbf{I}}\boldsymbol{\omega} + \sum_{m=1}^{N_m}\bar{\boldsymbol{\Gamma}}_m\dot{A}_m\right] &= \boldsymbol{\mathcal{C}}_G \\ \dot{\boldsymbol{\omega}}\boldsymbol{\Gamma} + \sum_{m=1}^{N_m}\left[\ddot{A}_m + 2\omega_m\xi\dot{A}_m + \omega_m^2 A_m\right] - \frac{1}{2}\boldsymbol{\omega}^T\mathbf{I}_1\boldsymbol{\omega} & \\ -\boldsymbol{\omega}^T\left(\sum_m^{N_m}\mathbf{I}_{2,m}A_m\right)\boldsymbol{\omega} + 2\boldsymbol{\omega}\sum_{m=1}^{N_m}\boldsymbol{\Xi}^m\dot{A}_m &= \boldsymbol{\mathcal{Q}}\end{aligned} \tag{6}$$

Table 2
Natural frequencies of the satellite model, found using MSC Nastran.

Mode	ω (Hz)	Mode	ω (Hz)
1	2.30	6	82.41
2	14.32	7	84.24
3	14.50	8	134.15
4	41.38	9	135.36
5	45.58	10	143.31

where

$$\mathcal{F}_G = -\frac{\mu}{|\mathbf{x}_0|^2}\left[M + \frac{1}{|\mathbf{x}_0|}\left[\tilde{\mathbf{p}} - \hat{k}^{\mathrm{T}}\hat{k}\tilde{\mathbf{p}}\right] + \frac{3}{2|\mathbf{x}_0|^2}\left[\mathrm{tr}(\tilde{\mathbf{I}})\hat{k} + 2\tilde{\mathbf{I}}\hat{k} - 5\hat{k}\left(\hat{k}^{\mathrm{T}}\tilde{\mathbf{I}}\hat{k}\right)\right]\right],$$
$$\mathcal{C}_G = -\frac{\mu}{|\mathbf{x}_0|^2}\left[\tilde{\mathbf{p}}\times\hat{k} - \frac{\hat{k}\times\tilde{\mathbf{I}}\hat{k}}{|\mathbf{x}_0|}\right],$$
$$\mathcal{Q} = -\frac{\mu}{|\mathbf{x}_0|^2}\left[\Lambda\hat{k} - \frac{\mathrm{tr}(\tilde{\mathbf{I}}_1)}{2|\mathbf{x}_0|} + \frac{15}{2|\mathbf{x}_0|^2}\left[\hat{k}\times\tilde{\mathbf{I}}_1\hat{k}\right]\right]. \tag{7}$$

Here, $\hat{k}$ is a vector in BRF that points towards $\hat{\mathbf{x}}_I$. The tilde notation ($\tilde{\bullet}$) denotes the deformation-dependent form of each mass property. Full definitions of the mass-dependence parameters are presented in Appendix B.

2.3. Structural model

The structural components of the satellite model are modelled using the MSC Nastran FE software package. The central rigid body is connected to two flexible solar panels that are modelled using quadrilateral plate elements (CQUAD4). The rigid connections that affix the two flexible appendages are added as massless Rigid Body Elements (RBE2), which fixes the translational and rotational displacements of the panel boundary nodes to those of the rigid body.

The dynamics of the system, as defined by Eqs. (6)–(23), are simulated in Matlab, with the natural frequencies ($\boldsymbol{\omega}$) found via the Modal Analysis step in Nastran. To facilitate this procedure, the connection between the rigid body and the solar panels are modelled using the Baumgarte stabilisation method [57], in which the algebraic kinematic constraints are transformed into differential form. The validity of this simplified approach was assessed through a separate modal analysis in which the central body was entirely defined using RBE2 elements, for which the agreement was within 10% (and much lower for higher modes) for all modes beyond the first, for which the antisymmetric mode differed by around 50%. This approach was taken to reduce the computational burden and does not impact the methodology itself. The first ten natural frequencies are presented in Table 2.

2.4. Validation

To validate that the approach outlined above is truly representative of the satellite dynamics, the system response is compared with results generated with the multibody dynamics software, MSC Adams. This software was selected based on its ability to combine rigid and flexible structural dynamics, as well as its fast simulation speed for complex problems. The system comprises a rigid central body and two flexible appendages, which are directly imported from Nastran. As such, the structural model, and subsequently frequency characteristics, are consistent between the two cases.

With this initial agreement validated, it was then possible to validate the system dynamics by comparing the responses, in Nastran and Adams, to a series of torques. Three torques of magnitude 0.1 Nm were applied in the main directions of the inertia tensor, so that the full set of DOFs could be investigated. These torques are displayed in Fig. 2. Fig. 3 presents the subsequent angular motion of the satellite, with Fig. 4

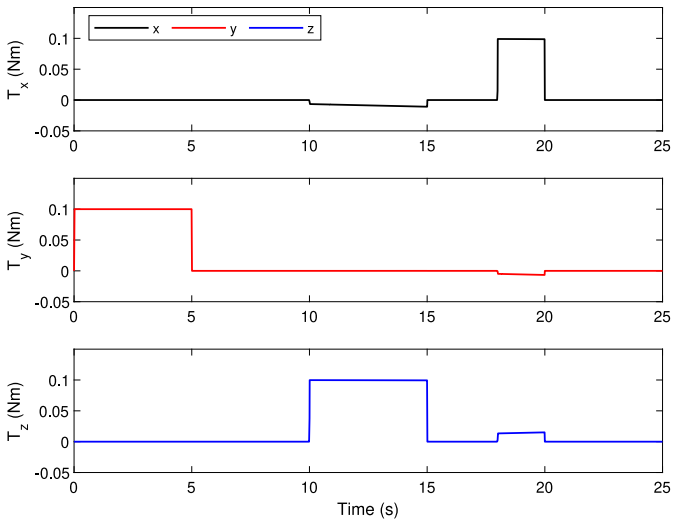

Fig. 2. Time history of the torque applied in the initial system identification.

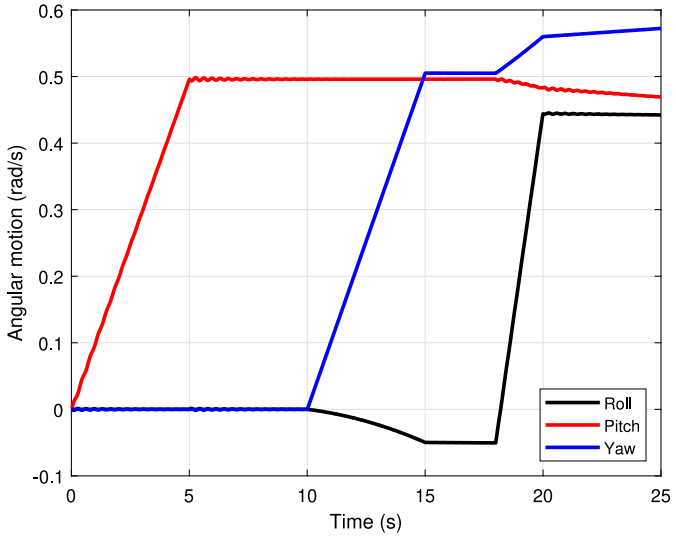

Fig. 3. Time history of the angular motion in the initial system identification.

Table 3
Percentage errors of the predicted moment of inertia values for Case 1.

Value	Error (%)
$I_{1,1}$	−0.864
$I_{2,2}$	−0.098
$I_{3,3}$	0.057

showing the absolute error in this prediction (relative to the reference results produced using Adams), which are shown to be of the order of 10^{-4}. The percentage error of the first modal displacement versus the Adams results are shown in Fig. 5, and are of the order of 10^{-5}%. As such, we conclude that the modelling approach outlined above is valid.

3. System identification and control

In this section, we outline the novel system identification strategy, which utilises DUKF to simultaneously estimate the kinematic state of the satellite and changes in the mass distribution of the plant model defined in Section 2. The sensors and actuators applied to this system are discussed below, followed by the DUKF implementation.

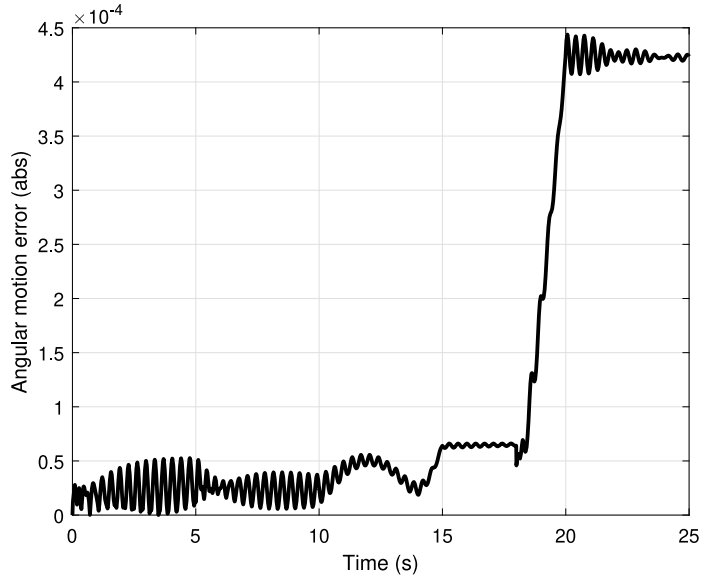

Fig. 4. Time history of the absolute error of the angular motion in the initial system identification.

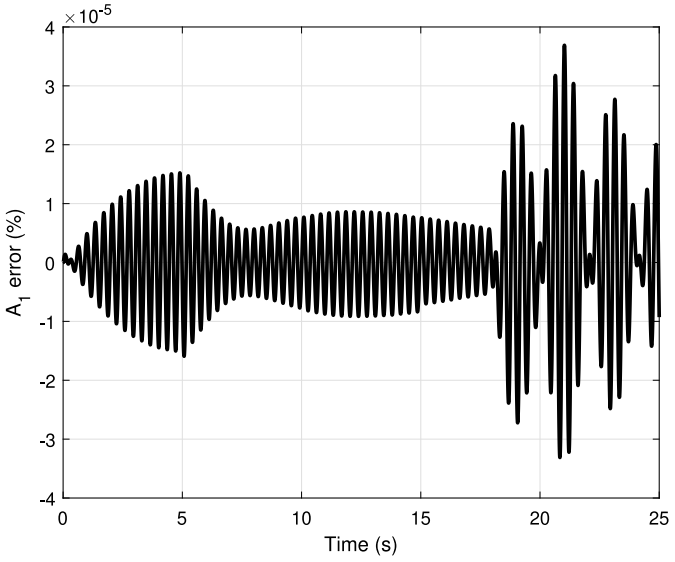

Fig. 5. Time history of the percentage error of the first modal displacement in the initial system identification.

3.1. System measurement

Three sensor types are utilised in this methodology: sun sensors, gyroscopes, and accelerometers. It should be noted that the integration of additional or alternative sensors could be integrated into this model without impacting the accuracy of the results.

3.1.1. Sun sensors

The sun sensors measure the angles of the satellite with respect to the sun position, which is assumed to be static. The two angles measure by the sun sensors, α and β are defined relative to the null position, in which the sun is along the boresight of the sensor, $\hat{s}_o = [0, 0, 1]^{\mathrm{T}}$. These angles are defined from the quaternion state, $\hat{Q}$, (measured by the sun sensors), as follows [58]:

$$\hat{s} = [\hat{s}_1, \hat{s}_2, \hat{s}_3]^{\mathrm{T}} = Q' \otimes \hat{s}_o \otimes Q, \tag{8}$$

$$\alpha = \tan^{-1}\left(\frac{\hat{s}_2}{\hat{s}_3}\right), \tag{9}$$

$$\beta = \tan^{-1}\left(\frac{-\hat{s}_1}{\hat{s}_3}\right), \tag{10}$$

where $\otimes$ denotes the quaternion multiplication operator. Two sun sensors are integrated to observe over 360°.

3.1.2. Gyroscope

The gyroscope complements the measurements from the sun sensor, measuring the angular rotation rate of the satellite. The model takes the angular velocity states of the satellite and adds a random Gaussian error based on the spectral noise of the sensor. Then, a bias is added to simulate sensor misalignment and calibration errors. The measured inertial rate, ω_{meas}, is, therefore, defined as

$$\omega_{\mathrm{meas}} = E\omega_{\mathrm{true}} + \omega_{\mathrm{bias}} + \omega_{\mathrm{noise}}, \tag{11}$$

Here, E denotes the scale factor error, ω_{true}, ω_{bias} is the constant null-bias (with peak magnitude of $0.1°/s$ per sensing axis), and ω_{noise} is a normally-distributed random noise signal with standard deviation $0.05°/s$ per sensing axis.

3.1.3. Accelerometers

Given that the structural deformation of the flexible appendages is defined primarily by the system mode shapes, it is important that the accelerometers used to capture their behaviour are properly placed. To optimise the performance of the control system, as well as to minimise cost, it is useful to determine the minimum number of sensors required to accurately capture the structural dynamics. This requires careful examination of the sensor placement and their ability to collectively capture multiple mode shapes.

In this study, a structural health monitoring (SHM)-inspired approach was used to optimally observe the physical states of the system. We applied the methodology defined in [59], which combines a modal assurance criterion (MAC) with an improved adaptive genetic algorithm (IAGA). The MAC is a statistical indicator that quantifies the agreement (between 0 and 1) between two modes shapes of the flexible system (which can be observed in Appendix A). The $\{i, j\}^{\mathrm{th}}$ element of the MAC matrix is defined as:

$$\mathrm{MAC}(i, j) = \frac{(\varphi_i^{\mathrm{T}}\varphi_j)^2}{(\varphi_i^{\mathrm{T}}\varphi_i)(\varphi_j^{\mathrm{T}}\varphi_j)}, \tag{12}$$

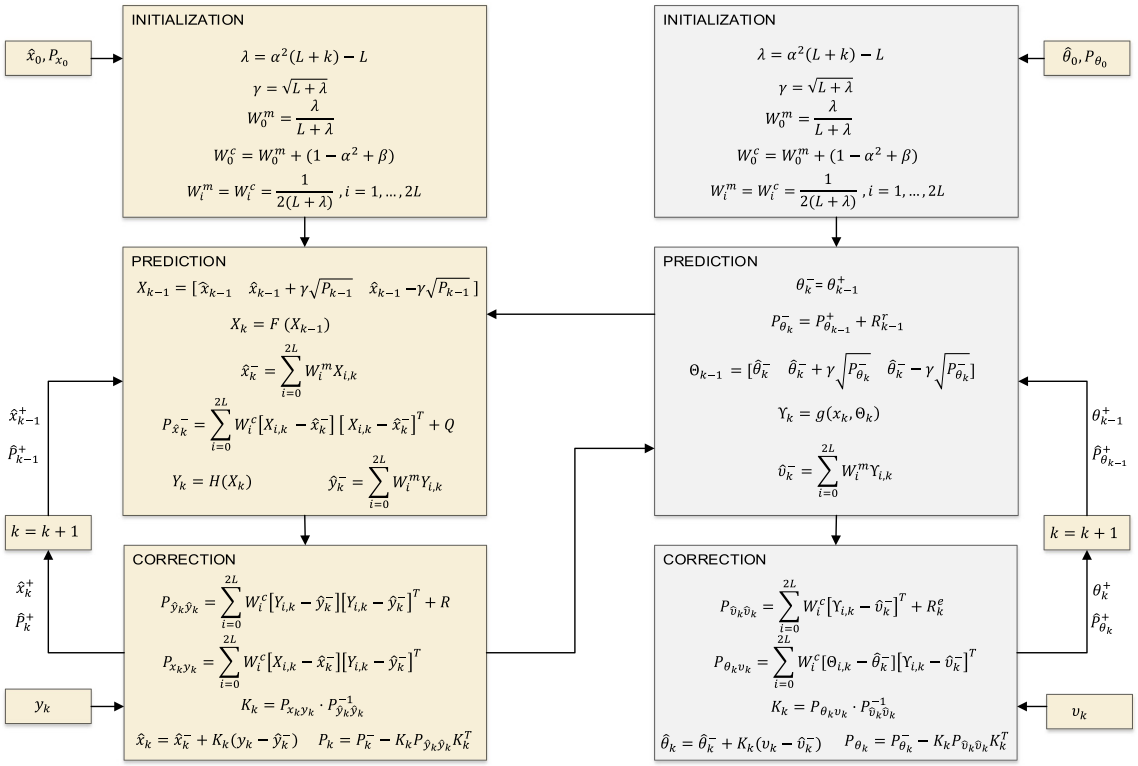

Fig. 6. Overview of DUKF approach.

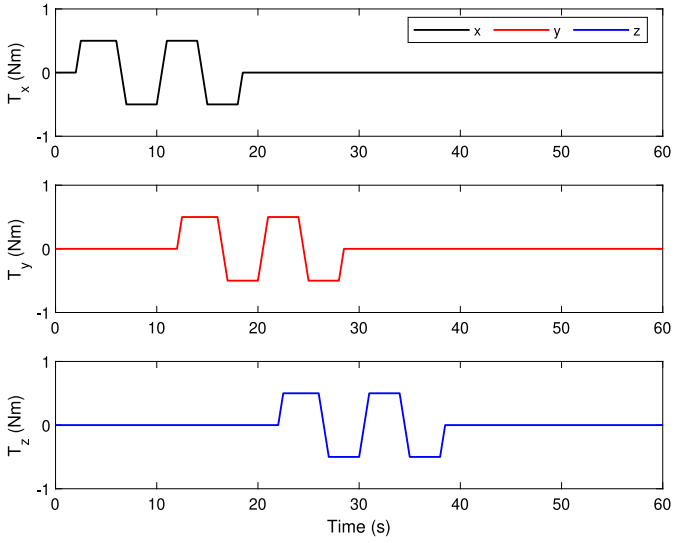

Fig. 7. Time history of the three-dimensional torque applied in Case 1.

where φ_k denotes the k^{th} structural mode, as captured by the accelerometers, referred to as "sensor modes". That is, in each iteration of the IAGA procedure, N nodes are assumed to have an accelerometer attached to them and the system response is recorded only at these N positions. This truncated recording of the full system response can be projected onto a similarly truncated "sensor mode" basis (i.e., the mode shapes recorded only at the N selected nodes) in the standard manner (i.e., if the response was recorded at all modes). Through this approach, it is possible to develop a MAC matrix that is dependent on the sensor positions. Through this procedure, it was decided that five accelerometers should be used, as this provided a balance between sufficient coverage of the structural dynamics and low cost.

3.1.4. Actuators

The system is actuated using momentum wheels, which manage the momentum of the satellite. The actuators were set to have a saturation torque of 0.05 Nms, update rate of 100 Hz, and minimum torque of 0.1 mNm. The actuator model is again implemented using Simulink, which begins when the torque is commanded and passed through a rate limiter to avoid high-torque differential peaks. A zero-order holder is implemented, followed by the addition of a lag to the actuator. Then, each torque is restrained in each direction by a saturation limiter. When the momentum wheel reaches its saturation point, the output torque is null. Before the torque is applied into the model, a threshold function sets the values of the torque below the minimum torque to zero.

4. DUKF-based system identification

In this section, we propose a novel system identification strategy, utilising dual Unscented Kalman filters (DUKF) to simultaneously calculate changes to the mass distribution and the kinematic state of the spacecraft.

The estimation of the states involves the nonlinear dynamic system in discrete time as follows:

$$\begin{aligned} x_{k+1} &= F(x_k, \upsilon_k), \\ y_k &= H(x_k, n_k), \end{aligned} \tag{13}$$

where x_k is the unobserved state vector at each iteration k, y_k is the observed signal, υ_{k-1} is the process noise, and n_{k-1} is the observation noise. The functions F and H are used for the nonlinear mapping of measurements and states, respectively.

The DUKF strategy aims to determine a nonlinear mapping, $G : x_k \longrightarrow y_k$, that maps the observed state to the unobserved signal. This function is assumed to be parameterisable by some vector, θ, so that it may be written as $y_k = G(x_k, \theta)$. This allows the new state space representation to be written as

$$\begin{aligned} \theta_k &= \theta_{k-1} + u_k, \\ y_k &= G(x_k, \theta_k) + e_k. \end{aligned} \tag{14}$$

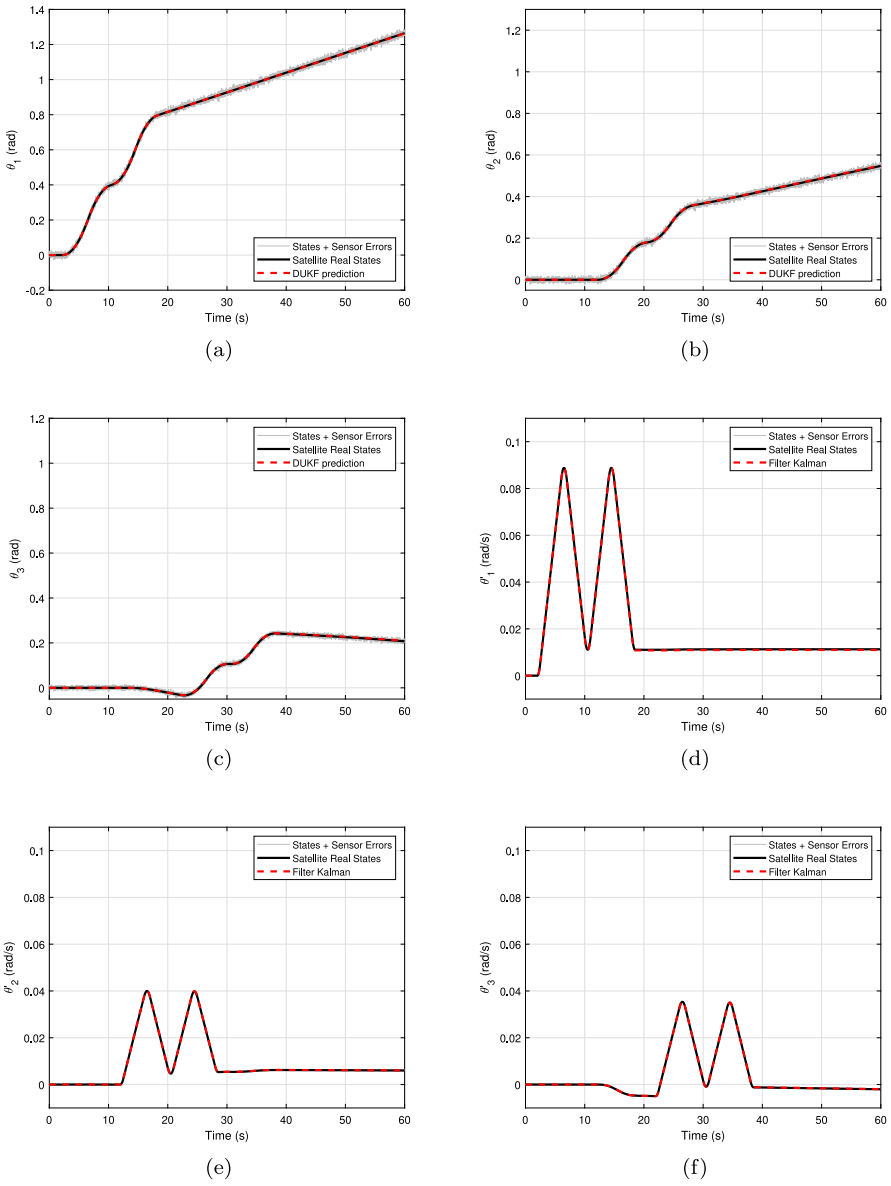

Fig. 8. Attitude predictions for Case 1.

Here, the parameters, θ, are dependent on the system state, and represent a stationary process that is driven by the process noise, u_k. The process error is denoted e_k.

The DUKF algorithm is divided into three key stages: initialisation, prediction, and correction. The UKF methodology assumes that there exists a set of points – named the *sigma points* – in the state space with probability density function similar to that of the system errors, with the implicit assumption that a probability function can be more readily approximated than an arbitrary nonlinear function. The random variable $\hat{x}$, with dimension L, is introduced, so that it may be propagated through the nonlinear function, G.

The selection of the sigma points depends on the initialisation parameters, and these are chosen so that their mean and covariance are $\bar{x} = \bar{\hat{x}}$ and $P_{\hat{x}}$, respectively. The filter is initialised with the known values of the initial state of the system, x_0, and its covariance, $P_0 = P(x_0)$. The scalar parameter $\lambda = \alpha^2(L + \kappa) - L$ is introduced, with α determining the dispersion of the sigma points around $\bar{x}$ (typically between 10^{-4} and 1), and λ a secondary scaling parameter that is typically set to 0 or $(3 - L)$ [60].

Then, the construction of the $2L + 1$ sigma vectors X_i (and corresponding weights, W_i) are defined by [61]

$$X_i = \bar{x} \pm (\sqrt{(L+\lambda)P_x})_i, \qquad i = 0, \dots, L, \tag{15}$$

$$W_0^m = \frac{\lambda}{L+\lambda}, \tag{16}$$

$$W_0^c = \frac{\lambda}{L+\lambda} + (1 - \alpha^2 + \beta), \tag{17}$$

$$W_i^m = W_i^c = \frac{1}{2(L+\lambda)}, \qquad i = 0, \dots, L. \tag{18}$$

Here, $(\sqrt{(L+\lambda)P_x})_i$ denotes the i^{th} row of the matrix square root, and the superscripts ^{m} and ^{c} represent the weightings for the mean and covariance, respectively. The parameter β is introduced to incorporate prior information regarding the distribution of $\bar{x}$; for Gaussian distributions, the optimal value is $\beta = 2$.

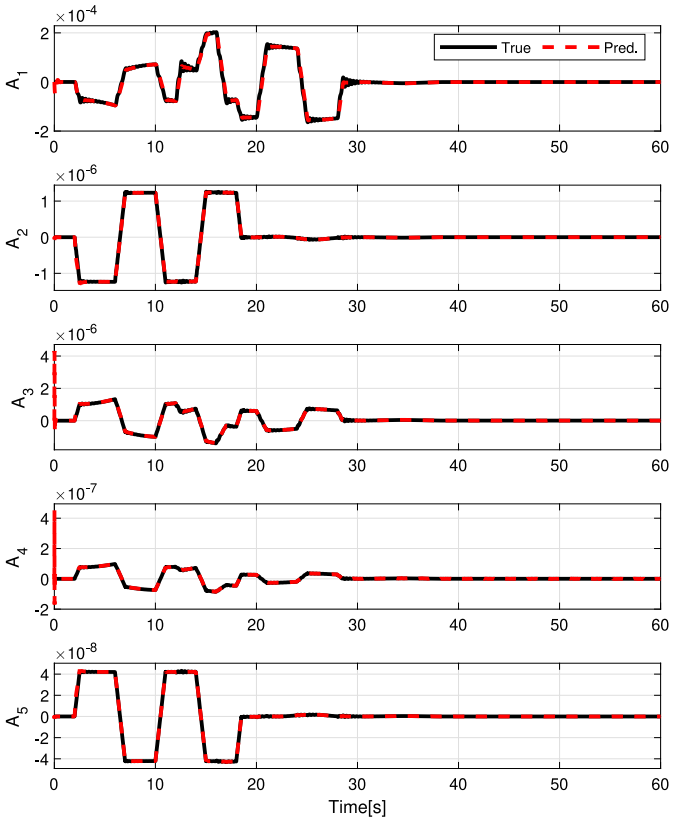

Fig. 9. Displacement predictions for the flexible appendage in Case 1.

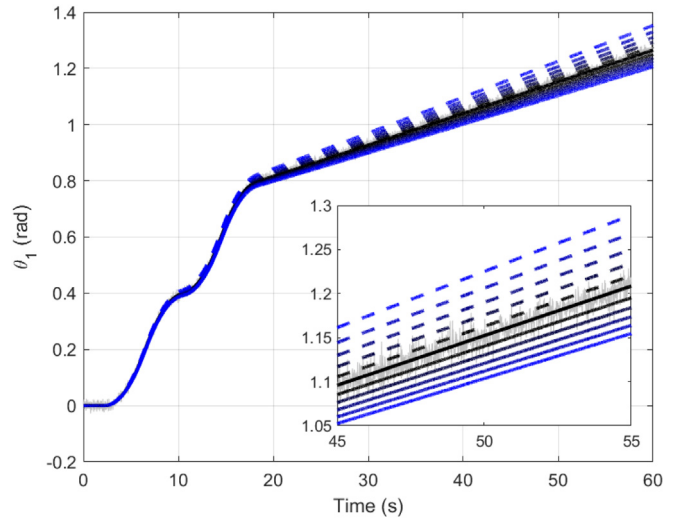

Fig. 10. Time history for θ_1, with the initial error in the value of $I_{1,1}$ ranging from −50% (blue dashed) to +50% (blue solid).

The prediction step forecasts the next iteration of the state by using the nonlinear mapping $X_k = F(X_{k-1}, V_{k-1})$. The predicted $(^-)$ system state and covariance can then be calculated from the sigma points and associated weightings as

$$\begin{aligned} \bar{x}_k^- &= \sum_{i=0}^{2L} W_i^m X_{k,i}, \\ P_{x,k}^- &= \sum_{i=0}^{2L} W_i^c [X_{k,i} - \bar{x}_k^-][X_{k,i} - \bar{x}_k^-]^{\mathrm{T}} + Q. \end{aligned} \tag{19}$$

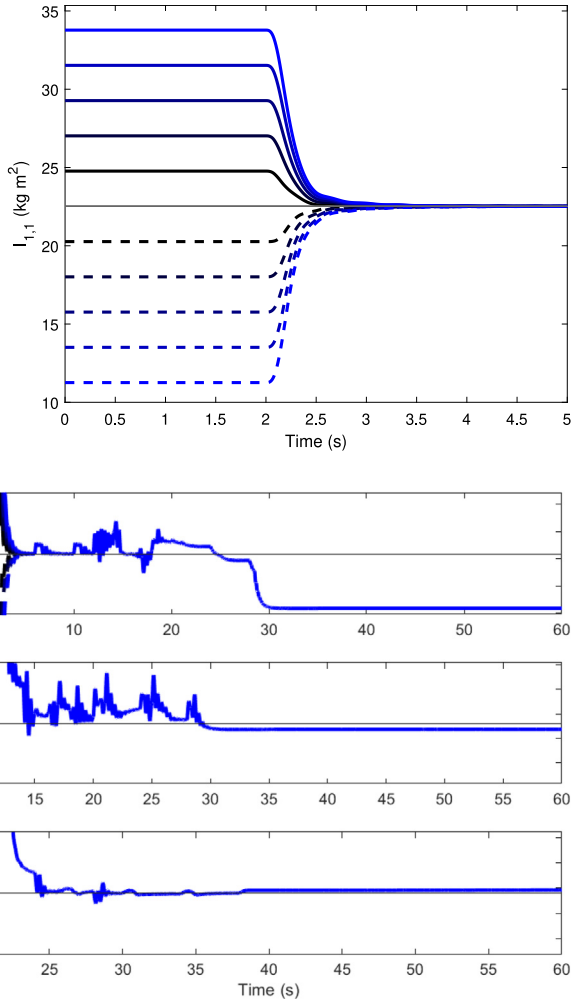

Fig. 11. Time histories for the diagonal values of the moment of inertia matrix, I, for Case 1. The first panel zooms in on the initial five second period for $I_{1,1}$, and the second set of panels shows the full time history for all three values. For each sub-panel, the y-axis interval is set to $(1 \pm 1\%)I_{n,n}$.

The prediction of the measurements can be found using $Y_k = H(X_k, N_k)$ for the sigma points and

$$\bar{y}_k^- = \sum_{i=0}^{2L} W_i^m Y_{k,i}, \tag{20}$$

for the full state.

Given the dual application of the UKF in this methodology, the parameterised function is updated in parallel. In this prediction step, Eq. (14) is used to update the parameters, based on the process noise, and parameterisation covariance.

The errors in the measurement prediction have been added as state variables in the cases when they are not purely additive noises. Although this complicates the computation of the problem – the size of state vector changes to $3L$, so the number sigma points becomes $(6L+1)$ – the non-additive noise better accepts large errors in the UKF [39].

The correction step begins by defining the covariance between the predicted states and measurements:

$$\begin{aligned} P_{y,y,k}^- &= \sum_{i=0}^{2L} W_i^c [Y_{k,i} - \bar{y}_k^-][Y_{k,i} - \bar{y}_k^-]^{\mathrm{T}} + R, \\ P_{x,y,k}^- &= \sum_{i=0}^{2L} W_i^c [X_{k,i} - \bar{x}_k^-][Y_{k,i} - \bar{y}_k^-]^{\mathrm{T}}. \end{aligned} \tag{21}$$

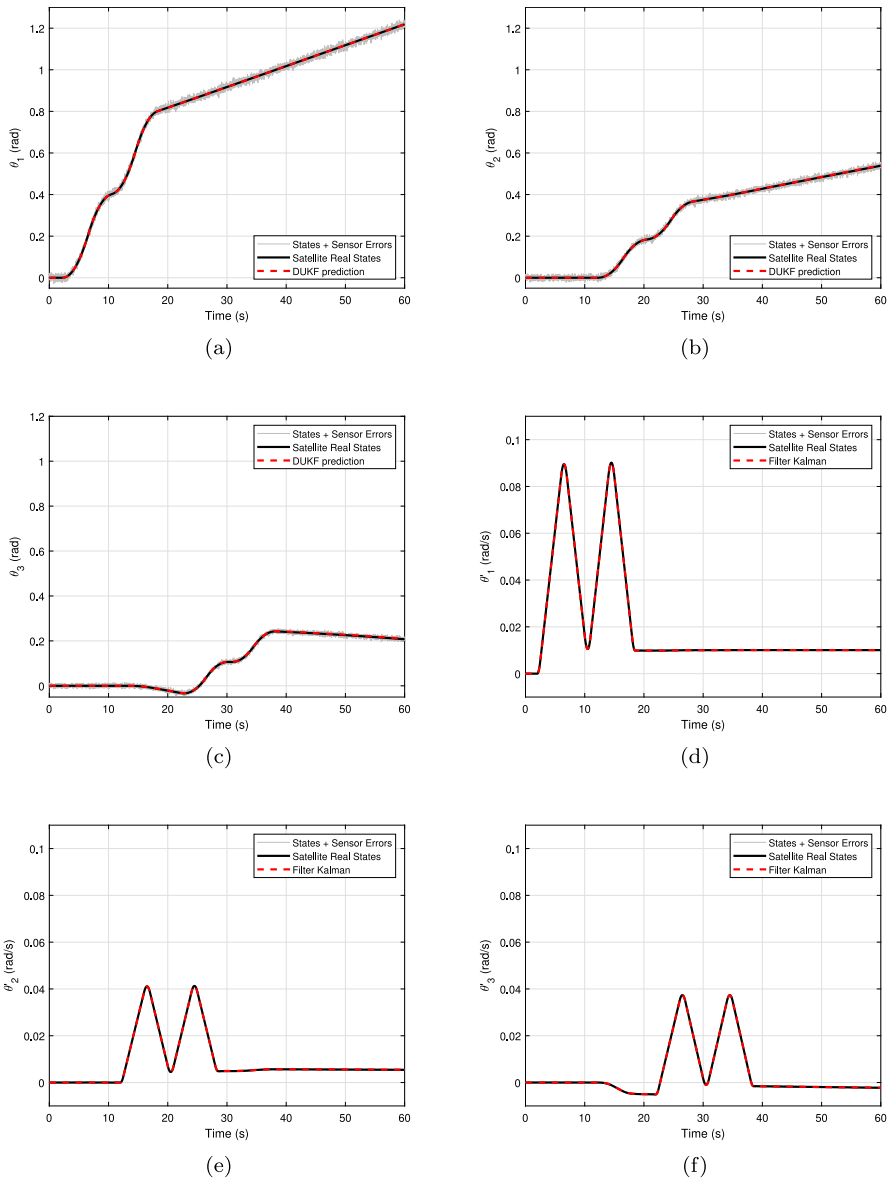

Fig. 12. Attitude predictions for Case 2, under the applied torque presented in Fig. 7.

Then, the correction of the predicted values are applied using the Kalman gain, $K_k = P_{x,y,k} P_{y,y,k}^{-1}$, which corrects the predicted states using a linear combination of the differences between the true and predicted measurements. This gain is then used to calculate the updated state and covariance:

$$\begin{aligned} \bar{x}_k &= \bar{x}_k^- + K_k(y_k - \bar{y}_k^-), \\ P_{x,k} &= P_{x,k}^- - K_k P_{y,y,k} K_k^{\mathrm{T}}. \end{aligned} \tag{22}$$

The procedure for updating the model parameterisation, θ, is comparable to that for the state model. The two UKFs, for the state and the parameters, iteratively feed into one another during each step; this procedure is outlined in Fig. 6. The updated parameters are used for the prediction of the states, which are then used to predict the subsequent measurement of the parameters. This interconnectedness enables us to improve the state correction and parameter calculation based on the measured responses inputted from the sensors measuring the attitude states and panel vibrations. Data from the actuators is also used in the DUKF for the estimation of the states.

5. Results

To assess the ability of these two methods to capture and control the combined satellite dynamics, we have designed two case studies:

- *Case 1: Mischaracterised initial moment of inertia.* In the first case, the model is initialised with an incorrect value for $I_{1,1}$, to explore its ability to correctly identify this parameter based on the measured data. In this study, the value of $I_{1,1}$ is varied by increments of 10%, though the observations are generalisable to the full matrix. The initial values of $I_{2,2}$ and $I_{3,3}$ are 5% above the true value to mimic scenarios in which terrestrial system identification is insufficient.
- *Case 2: Time-varying moment of inertia.* To mimic the changes in inertia that occur as fuel is utilised by the thrusters, the moment of inertia decays with time. Therefore, this case tests the ability of the methods to adaptively characterise and control the system. In this study, the fuel is assumed to be placed centrally around the centre of mass of the rigid body so that the centre of mass

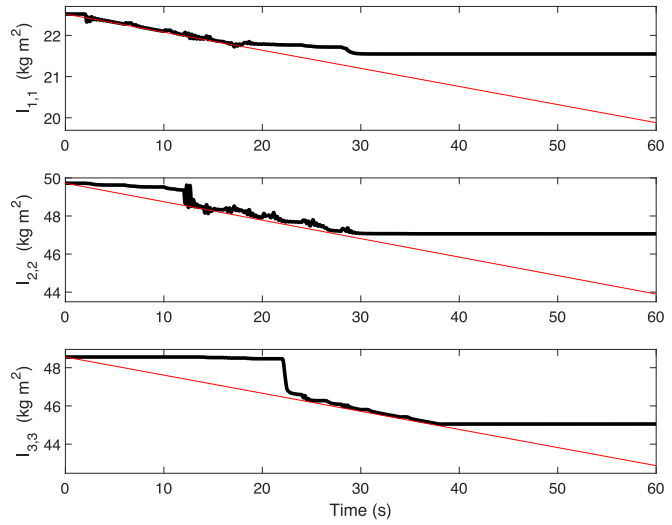

Fig. 13. Inertia predictions for the flexible appendage in Case 2, under the applied torque presented in Fig. 7. The true values are shown in red. (For interpretation of the references to colour in this figure legend, the reader is referred to the web version of this article.)

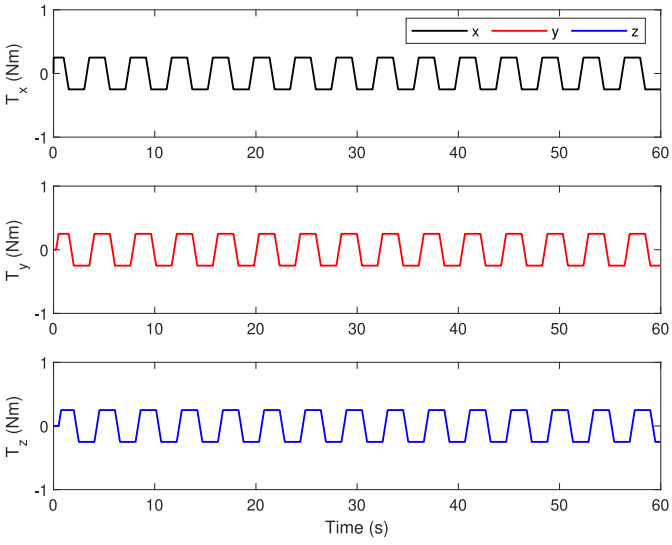

Fig. 14. Time history of the three-dimensional torque applied in Case 2.

does not require recalculation at each time step, though this can easily be added.

5.1. Case 1: Mischaracterised initial moment of inertia

As discussed above, Case 1 aims to investigate the ability of the DUKF approach to make in-orbit corrections to the predicted inertia properties, system based on sensor data. To actuate the system (and hence facilitate system identification through the DUKF algorithm), a three-dimensional, time-varying torque is applied; this is presented in Fig. 7. The predictions of the DUKF algorithm when the inertia properties are correctly tuned are presented in Fig. 8. It can be observed here that the predictions of both attitude and its derivative are very accurate. The structural vibrations of the first five sensor modes are displayed in Fig. 9, and the prediction is again shown to be accurate, with the predictions converging within a very small number of iterations.

The ability to accurately capture the system dynamics during orbit is dependent on the accuracy with which the inertial properties are captured. In particular, for robust application, the DUKF algorithm proposed must be able to correct errors in the characterisation of these properties in real time. Therefore, to simulate the scenario in which the initial characterisation of these properties is incorrect, the initial prediction of $I_{1,1}$ is perturbed by errors $e = \{\pm 10\%, \pm 20\%, \pm 30\%, \pm 40\%, \pm 50\%\}$. The time history predictions made by the DUKF algorithm for θ_1 and the diagonal (nonzero) values of the moment of inertia matrix are presented in Figs. 10 and 11, respectively. Note that the other components of the attitude time histories presented in Fig. 8, as well as the displacement time histories in Fig. 9 are not repeated as their accuracy was unaffected by the imposed error.

In Fig. 10, it can be observed that the dynamics of θ_1 are generally well captured by the DUKF algorithm, though there is a noticeable drift from the true solution with time that increases with the error level. Although somewhat concerning, it should be noted that the errors in the initial value of $I_{1,1}$ are specifically selected to be greater than those that should be expected if proper modelling procedures are followed.

From Fig. 11, it can be noted that the predicted value of $I_{1,1}$ does not change when there is no torque is applied to the system. However, once a torque is applied (at $t = 2$ s), the DUKF algorithm rapidly converges to an accurate value. Beyond this initial convergence, it can be observed that the system continues to update and correct the moment of inertia matrix as the applied torque changes. Further, the predicted values of $I_{2,2}$ and $I_{3,3}$ are invariant to the incorrect value of $I_{1,1}$. Across all three cases, the predicted values are not updated once the torque is set to zero, implying that the system will update its system identification as manoeuvres or other perturbations are applied.

The errors in the converged predictions for the moment of inertia matrix are presented in Table 3. It should be noted that the percentage error is below 1% across all three axis, which represents an improvement by an order of magnitude from previous in-orbit inertia identification strategies based on Kalman filters [49], suggesting a tangible benefit to the dual UKF strategy developed here.

5.2. Case 2: Time-varying moment of inertia

Case 2 aims to assess the ability of the DUKF algorithm to update the system identification when the mass and structural properties changes with time. It is important that any changes to the system can be accurately accounted for in both the system identification and control. For example, if the thrusters are used, fuel is spent, meaning that the mass of the rigid body – and hence the system properties that depend on mass – changes with time. To simulate these changes, the mass of the system in Case 2 decays at a rate of 1 kg/s. This is, of course, a highly exaggerated rate, but it allow the capabilities of the methodology to be assessed within a much shorter time frame. For the purposes of simplicity, the position of the fuel tank is assumed to be central, so that the centre of mass remains constant. In practice, this may not be the case, but the methodology can easily be adapted so that both the moment of inertia and centre of mass are recalculated at each time step.

The natural progression from Case 1 is to excite the system using the same torque presented in Fig. 7. While the attitude (Fig. 12) and structural dynamics were again captured accurately by the DUKF approach, the inertia predictions presented in Fig. 13 showed significant errors. Similarly to Case 1, the moment of inertia values are only updated when a torque is actively applied, and it can again be observed that the predicted value plateaus once the torque is no longer applied. Fig. 13 further demonstrates that an accurate update to the value of each $I_{n,n}$ only occurs when the torque is applied in the corresponding axis. To explore this phenomenon further, an extended, alternating torque – presented in Fig. 14 – is applied to the satellite. The predictions for the system attitude and structural dynamics are presented in

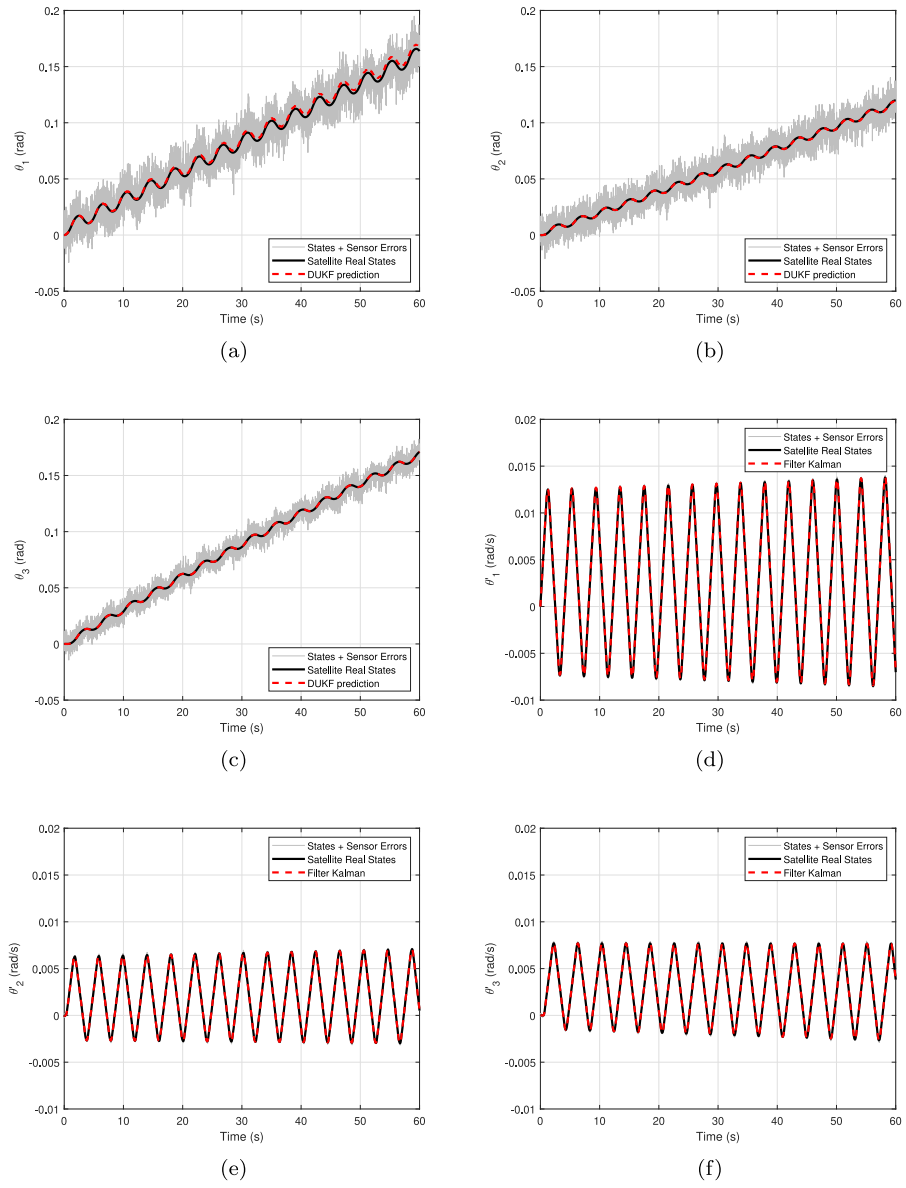

Fig. 15. Attitude predictions for Case 2.

Figs. 15 and 16, respectively, in which both are well captured. It should be noted that some of the higher frequency vibrations in Fig. 16 are slightly averaged, though this has not proven detrimental to the overall system identification.

In Fig. 17, the predictions of the diagonal values of the moment of inertia matrix are presented. In this figure, the deviation of the predicted moment of inertia values remain significantly closer to the true values, despite the exaggerated mass decay rate. In practice, when fuel is used and the mass changes as a result, the rate will be much lower, so the need for continuous torques will not be necessary and those applied by the AOCS will likely maintain an "acceptable" error in the inertia prediction, or one that can be easily remedied through small manoeuvres.

6. Conclusions

This paper presented a novel in-orbit system identification strategy for a small satellite, based on the application of a dual Unscented Kalman filter algorithm. The full system dynamics were derived based on a Lagrangian approach, which combines the system attitude and orbit dynamics with a structural model developed using the MSC Nastran FE software package. This software was used to derive the structural properties, so that they can be directly implemented in the analytical system dynamics without the need for temporal simulation. The accuracy of this approach was validated using the MSC Adams multibody dynamics software.

The state of the system is measured using three sensors, namely sun sensors, gyroscopes, and accelerometers. The optimal position for the accelerometers is defined through an improved adaptive genetic algorithm, based on the principles of structural health monitoring and the application of the modal assurance criterion. The efficacy of this strategy was demonstrated as the sensors were correctly placed away from the stationary points of the lower-frequency modes, and close to the solar panel edges, which will likely encounter the largest amplitudes of vibration.

The DUKF-based system identification strategy utilises two separate Unscented Kalman filters: one for the system state, the other for the parameterisation. This strategy allows for the continuous identification

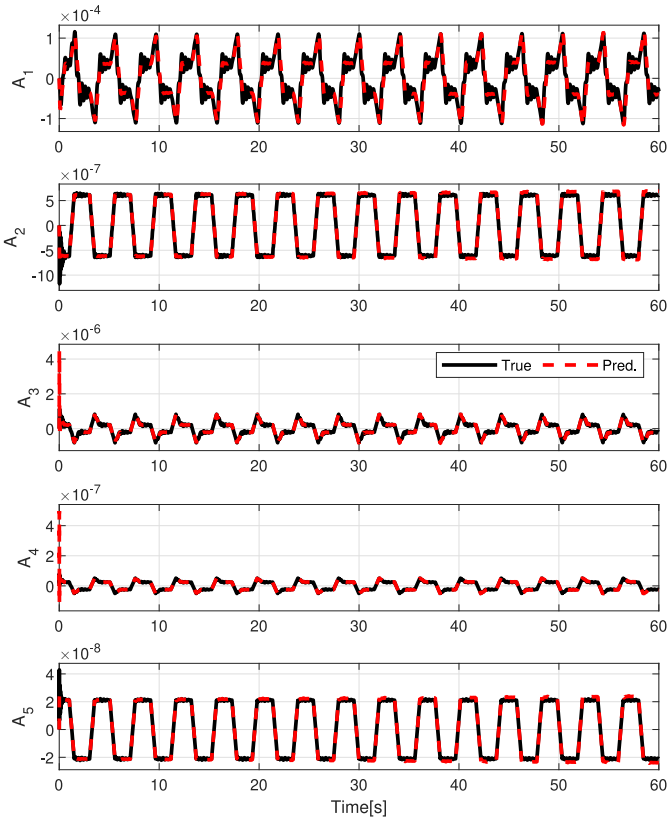

Fig. 16. Displacement predictions for the flexible appendage in Case 2.

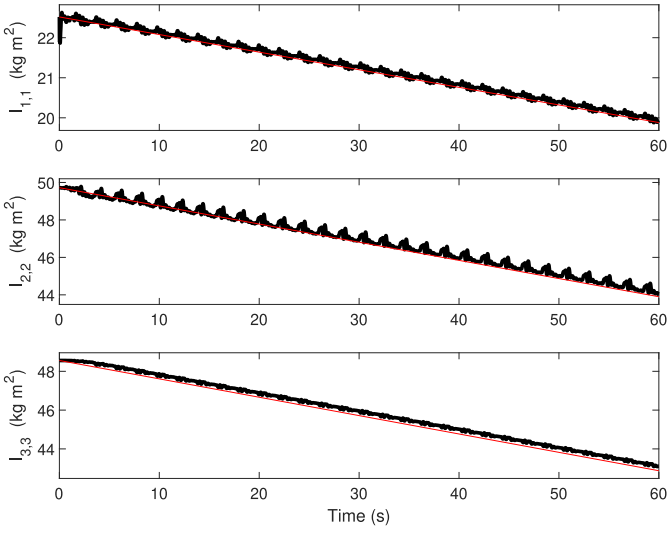

Fig. 17. Inertia predictions for the flexible appendage in Case 2. The true values are shown in red. (For interpretation of the references to colour in this figure legend, the reader is referred to the web version of this article.)

of the system. The accuracy of this approach was investigated using two distinct cases. In the first of these, the initial prediction of the moment of inertia matrix is intentionally chosen to be inaccurate, to mimic the scenario in which it is not possible to fully capture the exact values. The DUKF approach was able to converge upon an accurate value for $I_{1,1}$ (error less than 1%) within 2 s of simulated time, though only once a torque was applied. Further, the predicted values consistently returned to accurate values when perturbation were introduced through changes in the torque.

The second case aimed to assess the ability of the DUKF algorithm to update the values of the inertia matrix in the case these change with time, such as in the expenditure of fuel during thruster manoeuvres. To explore this, a highly exaggerated decay rate was applied to the system mass. We showed that updates to the predicted mass properties is only possible when an external perturbation, such as a torque, is applied to the system. This extreme case was further investigated through an active torque applied across the full time history, which demonstrated a significant increase in the predictions of the mass properties. Finally, it was concluded that, when this DUKF algorithm is applied in practice, it is highly likely that the inputs of the AOCS will be sufficient for an acceptable level of accuracy to be maintained during in-orbit operation.

CRediT authorship contribution statement

Alex J. Elliott: Writing – review & editing, Writing – original draft, Visualization, Validation, Software, Resources, Project administration, Methodology, Investigation, Formal analysis, Data curation. **Aydin Nakhaeezadeh Gutierrez:** Writing – review & editing, Visualization, Validation, Software, Resources, Methodology, Investigation, Formal analysis, Data curation, Conceptualization. **Leonard Felicetti:** Writing – review & editing, Writing – original draft, Supervision, Software, Resources, Project administration, Methodology, Investigation, Funding acquisition, Conceptualization. **Luca Zanotti Fragonara:** Writing – review & editing, Validation, Supervision, Project administration, Funding acquisition, Conceptualization.

Declaration of competing interest

The authors declare that they have no known competing financial interests or personal relationships that could have appeared to influence the work reported in this paper.

Appendix A. Flexible appendage mode shapes

In this section, the mode shapes corresponding to the first six natural frequencies are presented. Note that, due to the symmetry of the system, there are two mode shapes for each natural frequency, one for each solar panel. For Modes 3, 4, and 6, the stationary points are marked with a red circle (see Figs. 18–23).

Appendix B. Flexible appendage mode shapes

To simplify the following derivation of the dynamic equations, the following mass-dependence parameters are introduced:

$$
\begin{aligned}
M &= \int_V \rho dV, \\
\mathbf{p} &= \int_V \mathbf{d}\rho dV, \\
\tilde{\mathbf{p}} &= \mathbf{p} + \sum_{m=1}^{N_m} \boldsymbol{\Lambda}_k A_m, \\
\boldsymbol{\Lambda}_k &= \int_V \boldsymbol{\phi}_k \rho dV, \\
\boldsymbol{\Gamma}_k &= \int_V \mathbf{d} \times \boldsymbol{\phi}_k \rho dV, \\
\tilde{\mathbf{I}} &= \int_V (\mathbf{d}^{\mathrm{T}}\mathbf{d} - \mathbf{d}\mathbf{d}^{\mathrm{T}}) \rho dV = \quad \mathbf{I} + \sum_{m=1}^{N_m} \mathbf{I}_1^k A_k + \sum_{k,m=1}^{N_m} \mathbf{I}_2^{km} A_k A_m, \\
\tilde{\mathbf{I}}_1^k &= \mathbf{I}_1^k + 2 \sum_{m=1}^{N_m} \mathbf{I}_2^{km} A_m, \\
\boldsymbol{\Xi}^{km} &= \int_V \boldsymbol{\phi}_k \times \boldsymbol{\phi}_m \rho dV.
\end{aligned}
\tag{23}
$$

In Eq. (23), $\mathbf{I}$, $\mathbf{I}_1$, and $\mathbf{I}_2$ denote the moment of inertia, and its first and second variations, respectively.

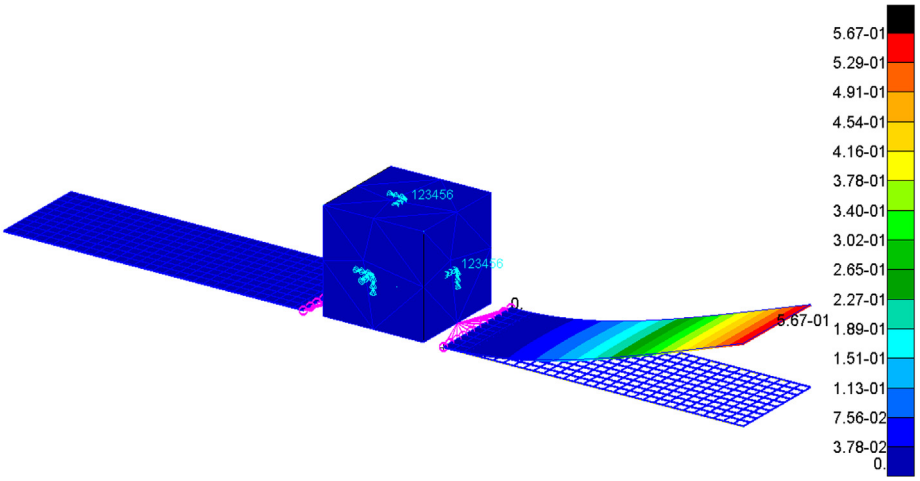

Fig. 18. Mode 1: first bending mode.

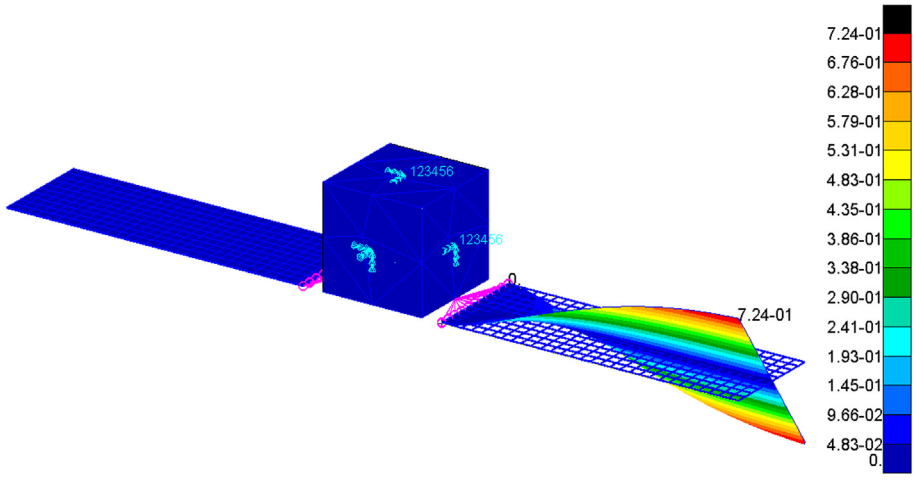

Fig. 19. Mode 2: first torsional mode.

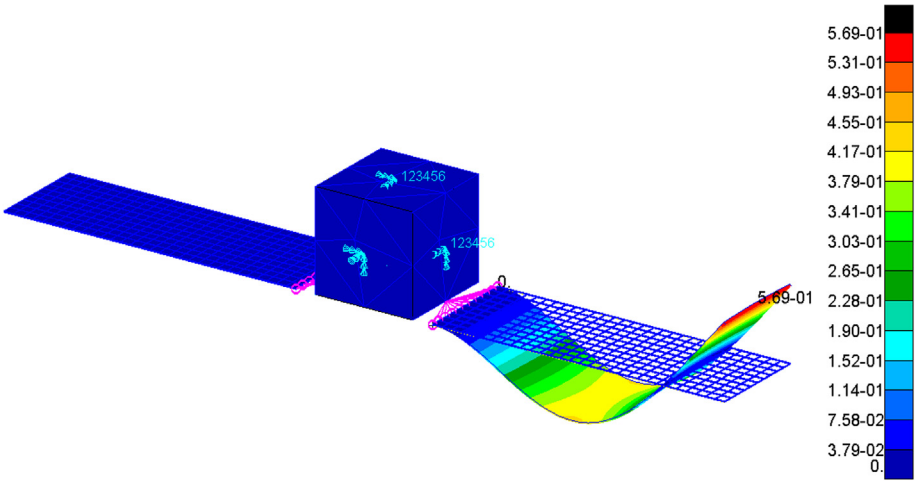

Fig. 20. Mode 3: second bending mode.

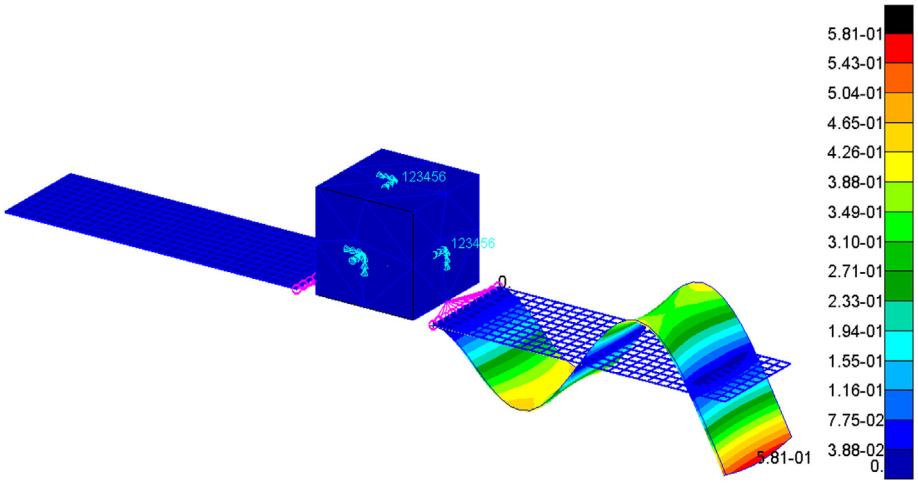

Fig. 21. Mode 4: third bending mode.

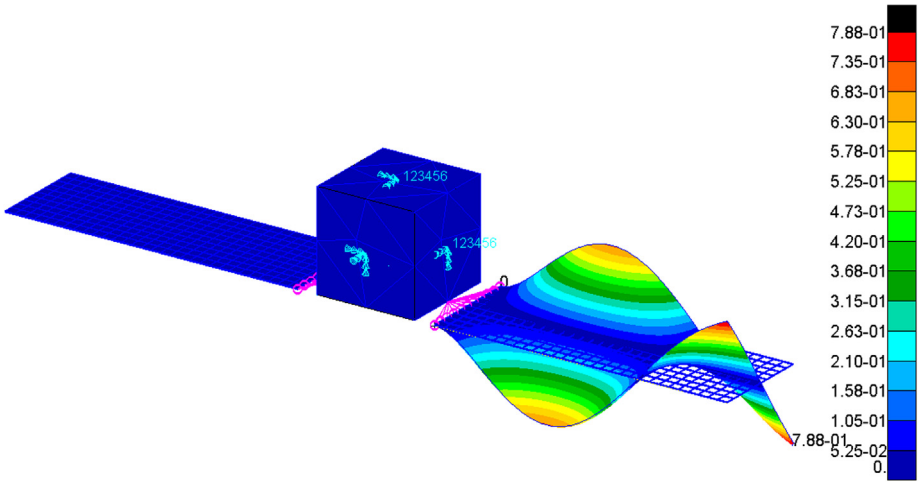

Fig. 22. Mode 5: second torsional mode.

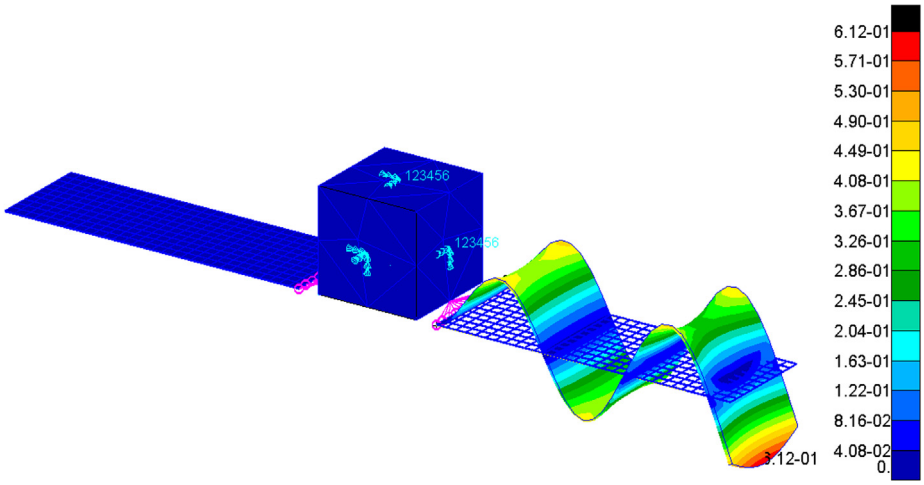

Fig. 23. Mode 6: fourth bending mode.

References

[1] M. Macdonald, V. Badescu, The International Handbook of Space Technology, Springer Berlin Heidelberg, 2014, pp. 1–731, http://dx.doi.org/10.1007/978-3-642-41101-4/COVER.

[2] V.J. Modi, Attitude dynamics of satellites with flexible appendages- A brief review, J. Spacecr. Rockets 11 (11) (1974) 743–751, http://dx.doi.org/10.2514/3.62172.

[3] Y. Hamed, K. Boulanouar, Y. Zhu, C. Han, Disturbance observer based anti-disturbance fault tolerant control for flexible satellites, Adv. Aircr. Spacecr. Sci. 5 (4) (2018) 459–475, http://dx.doi.org/10.12989/AAS.2018.5.4.459.

[4] M. Deng, H. Huang, Z. Li, B. Yue, Y. Lin, G. Liu, Coupling dynamics of flexible spacecraft filled with liquid propellant, J. Aerosp. Eng. 32 (5) (2019) 04019077, http://dx.doi.org/10.1061/(ASCE)AS.1943-5525.0001070.

[5] F. Angeletti, A. Stolfi, P. Gasbarri, Learning-based control of a spacecraft with sloshing propellant, Aerotec. Missili & Spazio 99 (1) (2020) 33–42, http://dx.doi.org/10.1007/s42496-020-00033-7.

[6] M. Stuttard, S. Amos, P. Aspden, M. Bowyer, C. Bridges, S. McLaren, Vast satcom antennas (VASANTs) as an enabling technology for commercial satellite communications, in: 16th Reinventing Space Conference, British Interplanetary Society, 2018, pp. 1–3, URL http://epubs.surrey.ac.uk/850828/, Paper no. BIS-RS-2018-04.

[7] G. Bodineaua, S. Bouladea, B. Fraparda, W.-H. Chenb, S. Salehic, F. Ankersenc, Robust control of large flexible appendages for future space missions, 2004.

[8] L. Mazzini, Flexible spacecraft dynamics, control and guidance: Technologies by Giovanni Campolo, in: Springer Aerospace Technology, Springer International Publishing, 2016, URL https://books.google.es/books?id=CKVJtAEACAAJ.

[9] I. Cash, CASSIOPeiA – A new paradigm for space solar power, Acta Astronaut. 159 (2019) 170–178, http://dx.doi.org/10.1016/J.ACTAASTRO.2019.03.063.

[10] R. Mu, S. Tan, Z. Wu, Z. Qi, Coupling dynamics of super large space structures in the presence of environmental disturbances, Acta Astronaut. 148 (2018) 385–395, http://dx.doi.org/10.1016/J.ACTAASTRO.2018.05.022.

[11] D. Wagg, S. Neild, Nonlinear Vibration with Control, vol. 218 (2015) http://dx.doi.org/10.1007/978-3-319-10644-1, URL https://link.springer.com/10.1007/978-3-319-10644-1.

[12] K. Lips, V. Modi, General dynamics of a large class of flexible satellite systems, Acta Astronaut. 7 (12) (1980) 1349–1360, http://dx.doi.org/10.1016/0094-5765(80)90011-9, URL http://www.sciencedirect.com/science/article/pii/0094576580900119.

[13] P. Santini, P. Gasbarri, Dynamics of multibody systems in space environment; Lagrangian vs. Eulerian approach, Acta Astronaut. 54 (1) (2004) 1–24, http://dx.doi.org/10.1016/S0094-5765(02)00277-1, URL http://www.sciencedirect.com/science/article/pii/S0094576502002771.

[14] F. Boyer, W. Khalil, M. Benosman, G. Vey, Modeling and control of flexible robots, in: Robot Manipulators. Modeling, Performance, Analysis and Control, 2010, pp. 337–394, http://dx.doi.org/10.1002/9780470612286.ch7.

[15] M. Tahmasebi, S.M. Esmailzadeh, Modeling and co-simulating of a large flexible satellites with three reaction wheels in ADAMS and MATLAB, Int. J. Dyn. Control 6 (1) (2018) 79–88, http://dx.doi.org/10.1007/s40435-016-0300-8.

[16] F. Amirouche, T. Jia, Modelling of clearances and joint flexibility effects in multibody systems dynamics, Comput. Struct. 29 (6) (1988) 983–991, http://dx.doi.org/10.1016/0045-7949(88)90324-0, URL http://www.sciencedirect.com/science/article/pii/0045794988903240.

[17] J. Deyst, A Survey of Structural Flexibility Effects on Spacecraft Control Systems, American Institute of Aeronautics and Astronautics (AIAA), 1969, http://dx.doi.org/10.2514/6.1969-116, URL https://arc.aiaa.org/doi/10.2514/6.1969-116.

[18] G.C. Marshall, F.J. Barbera, Attitude stability of spinning flexible spacecraft, 1971.

[19] P.M. Bainum, V.K. Kumar, The Dynamics and Control of Large Flexible Space Structure-III: The Modelling, Dynamics, and Stability of Large Earth Pointing Orbiting Structure, Final Report, NASA Grant: NSG-1414, Suppl. 2, Howard University, 1980.

[20] P.M. Bainum, A. Reddy, R. Krishna, C.M. Diarra, V.K. Kumar, The Dynamics and Control of Large Flexible Space Structure-V, Final Report, NASA Grant: NSG-1414, Suppl. 4, Howard University, 1982.

[21] W. He, S.S. Ge, Dynamic modeling and vibration control of a flexible satellite, IEEE Trans. Aerosp. Electron. Syst. 51 (2015) 1422–1431, http://dx.doi.org/10.1109/TAES.2014.130804.

[22] Q. Hu, G. Ma, Variable structure control and active vibration suppression of flexible spacecraft during attitude maneuver, Aerosp. Sci. Technol. 9 (2005) 307–317, http://dx.doi.org/10.1016/J.AST.2005.02.001.

[23] H. Liu, L. Guo, Y. Zhang, An anti-disturbance PD control scheme for attitude control and stabilization of flexible spacecrafts, Nonlinear Dynam. 67 (2012) 2081–2088, http://dx.doi.org/10.1007/S11071-011-0130-3/METRICS, URL https://link.springer.com/article/10.1007/s11071-011-0130-3.

[24] D.P. Madonna, M. Pontani, P. Gasbarri, Nonlinear attitude maneuvering of a flexible spacecraft for space debris tracking and collision avoidance, Acta Astronaut. 210 (2023) 268–288, http://dx.doi.org/10.1016/J.ACTAASTRO.2023.03.043.

[25] P. Gasbarri, R. Monti, M. Sabatini, Very large space structures: Non-linear control and robustness to structural uncertainties, Acta Astronaut. 93 (2014) 252–265, http://dx.doi.org/10.1016/J.ACTAASTRO.2013.07.022.

[26] P. Gasbarri, M. Sabatini, A. Pisculli, Dynamic modelling and stability parametric analysis of a flexible spacecraft with fuel slosh, Acta Astronaut. 127 (2016) 141–159, http://dx.doi.org/10.1016/j.actaastro.2016.05.018.

[27] R. Gordon, K. Worrall, M. Ceriotti, Attitude control of satellites with flexible appendages using inverse simulation, in: 72nd International Astronautical Congress 2021, Dubai, United Arab Emirates, 25-29 Oct 2021, 2021, pp. 833–847.

[28] R. Gordon, M. Ceriotti, K. Worrall, Attitude control of satellites with flexible appendages using inverse simulation, in: 73rd International Astronautical Congress, IAC, Paris, France, 18-22 Sept 2022, 2022.

[29] L. Cao, B. Xiao, M. Golestani, Robust fixed-time attitude stabilization control of flexible spacecraft with actuator uncertainty, Nonlinear Dynam. 100 (2020) 2505–2519, http://dx.doi.org/10.1007/S11071-020-05596-5/FIGURES/14, URL https://link.springer.com/article/10.1007/s11071-020-05596-5.

[30] M. TayyebTaher, S.M. Esmaeilzadeh, Model predictive control of attitude maneuver of a geostationary flexible satellite based on genetic algorithm, Adv. Space Res. 60 (2017) 57–64, http://dx.doi.org/10.1016/J.ASR.2017.03.013.

[31] P. Iannelli, F. Angeletti, P. Gasbarri, A model predictive control for attitude stabilization and spin control of a spacecraft with a flexible rotating payload, Acta Astronaut. 199 (2022) 401–411, http://dx.doi.org/10.1016/J.ACTAASTRO.2022.07.024.

[32] O. Ma, H. Dang, K. Pham, On-Orbit Identification of Inertia Properties of Spacecraft Using a Robotic Arm, vol. 31, American Institute of Aeronautics and Astronautics Inc., 2012, pp. 1761–1771, http://dx.doi.org/10.2514/1.35188, URL https://arc.aiaa.org/doi/10.2514/1.35188.

[33] C. Wei, Y. Zhang, H. Wang, Y. Zhao, L. Zhang, Inertia Parameter Identification of Space Floating Target During Robotic Exploratory Grasping, vol. 233, SAGE PublicationsSage UK: London, England, 2019, pp. 4247–4260, http://dx.doi.org/10.1177/0954410018819567, URL https://journals.sagepub.com/doi/pdf/10.1177/0954410018819567?casa_token=pIEeiiRjhtIAAAAA%3AH6xxPo6xj2YurAn0xhUx2Mf7_Q1igOjMr0Kgb-93L78Gt4t008_ZIirnn8RG0pw3qftCRDE8SscA.

[34] C. Nainer, H. Garnier, M. Gilson, C. Pittet, In-orbit data driven identification of satellite inertia matrix, IFAC-PapersOnLine 51 (2018) 467–472, http://dx.doi.org/10.1016/J.IFACOL.2018.09.189.

[35] Deep learning-based inertia tensor identification of the combined spacecraft, 234, 2020, http://dx.doi.org/10.1177/0954410020904555.

[36] S. Schwunk, S. Straub, M. Jung, S. Wang, X. Jia, P. Takyi-Aninakwa, al, Q. Lai, H.-H. Zhang, G. Zhao, H. Zhou, T. Sheng, Identification method of moment of inertia with the observed angular velocity containing Gauss white noise, J. Phys. Conf. Ser. 2029 (2021) 012097, http://dx.doi.org/10.1088/1742-6596/2029/1/012097, URL https://iopscience.iop.org/article/10.1088/1742-6596/2029/1/012097 https://iopscience.iop.org/article/10.1088/1742-6596/2029/1/012097/meta.

[37] R.E. Kalman, A new approach to linear filtering and prediction problems, Trans. ASME–J. Basic Eng. 82 (Series D) (1960) 35–45.

[38] G.L. Smith, S.F. Schmidt, L.A. McGee, Application of statistical filter theory to the optimal estimation of position and velocity on board a circumlunar vehicle, NASA-TR-R-135, 1962, NASA Technical Report (TR).

[39] E. Wan, R. Merwe, The unscented Kalman filter for nonlinear estimation, 153–158, ISBN: 0-7803-5800-7, 2000, pp. 153–158, http://dx.doi.org/10.1109/ASSPCC.2000.882463.

[40] A. Trigolo, L. Souza, H. Kuga, Kalman filter application for flexible space system parameter identification, 2003.

[41] E.P. Babcock, E.P. Babcock, T. Bretl, CubeSat attitude determination via Kalman filtering of magnetometer and solar cell data, in: 25 th Annual AIAA/USU Conference on Small Satellites.

[42] D.Y. Dube, S.N. Sharma, H.G. Patel, Extended Kalman filter based estimations for satellite attitude control system, Int. J. Eng. Adv. Technol. (IJEAT) (2021) 2249–8958, http://dx.doi.org/10.35940/ijeat.E2592.0610521, URL www.ijeat.org.

[43] L. He, H. Zhou, G. Zhang, Improving Extended Kalman Filter Algorithm in Satellite Autonomous Navigation, vol. 231 (2016) 743–759, http://dx.doi.org/10.1177/0954410016641708, URL https://journals.sagepub.com/doi/pdf/10.1177/0954410016641708.

[44] H.E. Soken, C. Hajiyev, S.-I. Sakai, Robust Kalman filtering for small satellite attitude estimation in the presence of measurement faults, Eur. J. Control 20 (2014) 64–72, http://dx.doi.org/10.1016/j.ejcon.2013.12.002.

[45] Z. Qiu, H. Qian, G. Wang, Adaptive robust cubature Kalman filtering for satellite attitude estimation, Chin. J. Aeronaut. 31 (2018) 806–819, http://dx.doi.org/10.1016/J.CJA.2018.01.023.

[46] M. Ghani, N. Assadian, R. Varatharajoo, Attitude and deformation coupled estimation of flexible satellite using low-cost sensors, Adv. Space Res. 69 (2022) 677–689, http://dx.doi.org/10.1016/J.ASR.2021.08.010.

[47] Y. Shen, Y. Xu, X. Sheng, X. Yin, Kalman Filter Identification Method for Micro-Vibration Transfer Paths of Satellites, vol. 236, SAGE PublicationsSage UK: London, England, 2021, pp. 2194–2205, http://dx.doi.org/10.1177/09544100211053306, URL https:

//journals.sagepub.com/doi/pdf/10.1177/09544100211053306?casa_token=xQ1HijhkATMAAAAA%3A0-32kdZbXAlOkdRmZb8ZDTZxI8v7sa409GuUE-ypkiyGreW3FcPagp57vPsikqX3qcLJksFEp-aG.

[48] Y. Xu, Q. Hu, X. Shao, Composite adaptive attitude control for combined spacecraft with inertia uncertainties, Aerosp. Sci. Technol. 131 (2022) 107984, http://dx.doi.org/10.1016/J.AST.2022.107984.

[49] R. Liu, J. Zhou, M. Chi, G. Li, J. Zhang, Large-Scale Flexible Spacecraft Mass Properties Determination Using Torque-Generating Control, vol. 235, SAGE PublicationsSage UK: London, England, 2021, pp. 2033–2046, http://dx.doi.org/10.1177/0954410020988466, URL https://journals.sagepub.com/doi/pdf/10.1177/0954410020988466?casa_token=DJFbWGRivY4AAAAA%3AqxU5n2eekR5v2FJpCLR-sU81RTgG_csfNkpRQ_3s90CCth1emwMyEeL6b7D_YtdqaFP65YqY1gO-.

[50] M. VanDyke, J. Schwartz, C. Hall, Unscented Kalman filtering for spacecraft attitude state and parameter estimation, Adv. Astronaut. Sci. 119 (2004).

[51] L. Cao, W. Yang, H. Li, Z. Zhang, J. Shi, Robust double gain unscented Kalman filter for small satellite attitude estimation, Adv. Space Res. 60 (2017) 499–512, http://dx.doi.org/10.1016/J.ASR.2017.03.014.

[52] J. Xu, Y. Jing, G.M. Dimirovski, Y. Ban, Two-stage unscented Kalman filter for nonlinear systems in the presence of unknown random bias, in: 2008 American Control Conference, 2008, pp. 3530–3535, http://dx.doi.org/10.1109/ACC.2008.4587040.

[53] X. Chen, Two-stage unscented Kalman filter algorithm for fault estimation in spacecraft attitude control system, IET Control Theory Appl. 12 (2018) 1781–1791(10). URL https://digital-library.theiet.org/content/journals/10.1049/iet-cta.2017.1369.

[54] O. Rezaei, A. Rahdan, S. Sardari, M. Dahmardeh, Z. Wang, A fuzzy robust two-stage unscented Kalman filter method for uncertainty and state of charge estimation of lithium-ion batteries, J. Energy Storage 68 (2023) 107883, http://dx.doi.org/10.1016/j.est.2023.107883, URL https://www.sciencedirect.com/science/article/pii/S2352152X2301280X.

[55] M.I. Uddin, L. Zhang, Q. Xiao, H. Wang, Y. Hou, Two-stage Cubature Kalman filtering based on T-Transform and its application, Complexity 2021 (2021) 5538414, http://dx.doi.org/10.1155/2021/5538414.

[56] L. Zhang, A. Bagwari, G. Huang, Target tracking algorithm using two-stage Cubature Kalman filter, J. Intell. Syst. Control (2023) http://dx.doi.org/10.56578/jisc020405.

[57] J. Baumgarte, Stabilization of constraints and integrals of motion in dynamical systems, Comput. Methods Appl. Mech. Engrg. 1 (1) (1972) 1–16, http://dx.doi.org/10.1016/0045-7825(72)90018-7, URL https://www.sciencedirect.com/science/article/pii/0045782572900187.

[58] M.J. Sidi, Spacecraft Dynamics and Control: A Practical Engineering Approach, in: Cambridge Aerospace Series, Cambridge University Press, 1997.

[59] C. He, J. Xing, J. Li, Q. Yang, R. Wang, X. Zhang, A new optimal sensor placement strategy based on modified modal assurance criterion and improved adaptive genetic algorithm for structural health monitoring, Math. Probl. Eng. 2015 (2015) 626342, http://dx.doi.org/10.1155/2015/626342.

[60] S.J. Julier, J.K. Uhlmann, H.F. Durrant-Whyte, A new approach for filtering nonlinear systems, in: Proceedings of 1995 American Control Conference - ACC'95, Vol. 3, 1995, pp. 1628–1632.

[61] E.A. Wan, R. Van Der Merwe, The unscented Kalman filter for nonlinear estimation, in: Proceedings of the IEEE 2000 Adaptive Systems for Signal Processing, Communications, and Control Symposium (Cat. No.00EX373), 2000, pp. 153–158.

https://dspace.org/

In-orbit system identification of a flexible satellite with variable mass using dual Unscented Kalman filters

Elliott, Alex J.; Gutierrez, Aydin Nakhaeezadeh; Felicetti, Leonard; Fragonara, Luca Zanotti

2025-01
Elsevier
https://doi.org/10.1016/j.actaastro.2024.11.014
Elliott AJ, Gutierrez AN, Felicetti L, Fragonara LZ. (2024) In-orbit system identification of a flexible satellite with variable mass using dual Unscented Kalman filters. Acta Astronautica, Volume 226, Part 2, January 2025, pp. 71-86

Downloaded from a DSpace repository. https://dspace.org/